 doi:10.20944/preprints202207.0410.v1

Article

Detection of Waste Plastics in the Environment: Application of Copernicus Earth Observation Data

Samantha Lavender [1*]

[1] Pixalytics Ltd, Plymouth Science Park, Davy Road, Plymouth, United Kingdom, PL1 3DG 1; slavender@pixalytics.com
* Correspondence: slavender@pixalytics.com

Abstract: The detection of waste plastics in the marine and terrestrial environment using satellite Earth Observation data offers the possibility of large-scale mapping, and reducing on-the-ground manual investigation. In addition, costs are kept to a minimum by utilizing free-to-access Copernicus data. A Machine Learning based classifier was developed to run on Sentinel-1 and -2 data. In support of the training and validation, a dataset was created with terrestrial and aquatic cases by manually digitizing varying landcover classes alongside plastics under the sub-categories of greenhouses, plastic, tyres and waste sites. The trained classifier, including an Artificial Neural Network and post-processing decision tree, was verified using five locations encompassing these different forms of plastic. Although exact matchups are challenging to digitize, the performance has generated high accuracy statistics, and the resulting land cover classifications have been used to map the occurrence of plastic waste in aquatic and terrestrial environments.

Keywords: plastic; tyres; waste; greenhouses; remote sensing; Copernicus; Sentinel-1; Sentinel-2

1. Introduction

The presence of plastics in the environment is of increasing concern and a pressing environmental issue with incorrect disposal resulting in the contamination of marine, terrestrial and airborne environments. In addition, when plastics are exposed to ambient solar radiation, they slowly disintegrate into microplastics and release greenhouse gases, methane and ethylene [1]. Some facts of concern are that [2]: half of all manufactured plastics have been made in the last 15 years, and production has increased exponentially, from 2.3 million tons in 1950 to 448 million tons by 2015. Also, the mass of plastics is twice that of animate creatures inhabiting planet earth [3]. With an awareness of how plastic harms the environment, its mapping and recovery is an increasing focus alongside using less plastic in our everyday lives.

The everyday use of plastic bags and other single-use plastic products is widespread in many countries. Also, countries can have specific sources of plastics; e.g., in Nigeria, the packaging of drinking water in plastic is omnipresent [4]. Combined with this, waste management can be a significant problem due to a lack of recycling infrastructure, trained workforce, and other related factors. In addition, where facilities are available illegal fly-tipping can occur when those involved try to avoid disposal fees, e.g., the fly-tipping statistics for England in 2020/21 compared to 2019/20 showed a 16% increase with the primary source being household waste [5]. Additional concerns have arisen concerning waste materials being wrapped in plastics and disguised as other forms of legal waste, such as silage bales, which increases the difficulty of illegal waste detection and regulation enforcement [6,7].

In agriculture, plastics have become indispensable and are highly visible when used for crop protection and shading, such as greenhouses and ground covering films, and large plastic bales holding silage – termed plasticulture. However, in Europe, there are

 doi:10.20944/preprints202207.0410.v1

often inefficient management schemes, with data on the use of plastics in agriculture challenging to obtain [8].

Stockpiles of waste tyres have been identified as a significant danger to human and environmental health [6]. Before the introduction of the European Union's Waste Framework Directive (2008/98/EC) [9], it was estimated over a billion tyres existed in poorly managed or unmanaged stockpiles across Europe [10]. Globally, it is estimated that one billion end-of-life tyres are created annually, and approximately four billion are in stockpiles and landfills [11].

The environmental harm caused by waste plastics is not only to the location where the plastics are used/dumped, as they can end up in waterways that take them out to sea. During their transport in aquatic systems, fresh plastics are gradually broken down into microplastics (<5 mm in diameter) and nanoplastics (<1 μm) [12]. It is estimated that about 150 million tonnes of plastic debris circulate in the world's oceans [13].

Earth Observation (EO) data has the potential to detect plastics as they have a spectral signature that can be separated from the surrounding land cover types. For plastic waste floating on water, both Biermann et al. [14] and Themistocleous et al. [15] used indices derived from Sentinel-2 data; the Floating Debris Index and Plastic Index use the near-infrared (NIR) and red bands. The advantage of floating plastic is that the plastics are bright compared to the background, which is no longer true when plastics are on land as the background landcover can also have variable bright targets such as reflective roofs. Also, separating the detection of waste from the intended presence of plastics in the terrestrial environment can be difficult as it is present in greenhouses, synthetic turf and on the rooves of buildings as plastic roof tiles.

Amongst 33 polymers reported in the Indian coastal environment, polyethylene and polypropylene were the most dominant type in the sediment, water, and biota [16]. In plasticulture, polyethylene is popular as it's a white semitransparent plastic with a spectral reflectance strongly influenced by the soil/vegetation characteristics it covers. However, plastic-mulched farmland is brighter, smoother (because it reduces soil roughness) and drier (it has low vapor and air permeability and low water absorbability) than other classes. So, the reflectance of plastic-mulched farmland has higher reflectance values in the shortwave infrared (SWIR) bands [17]. Levin et al. [18] used absorption features at 1 218 and 1 732 nm to detect plastic features associated with plasticulture. Similarly, for floating plastic waste, Goddijn-Murphy and Dufaur [19] noted absorption peaks at around 1 140 and 1 680 nm.

Guffogg et al. [20] noted that an obstacle for spectral detection on some beaches was that a large percentage of the plastic debris was shoes, predominantly flip flops, with polyurethane foam not having received as much focus as other plastics. They found that between 2–8%, depending on the plastic polymer, of a unit area must be covered in plastics before the material can be spectrally separated from a non-contaminated area only containing sand.

The detection of municipal or illegal waste sites on land has received less attention, although they are a recognized source of poorly managed marine pollution. Page et al. [21] is the previous version of this paper's approach, which classified tyre and plastic waste in Scotland using Sentinel-1 and Sentinel-2 data. Kruse et al. [22] focused on plastic aggregation sites across Indonesia. They found that the centers of 19% of waste sites in Southeast Asia are located within 200 meters of a waterway or waterbody listed on OpenStreetMap, and more than half are within 750 m. Gill et al. [23] used Landsat thermal data due to the heat generation in landfills; in comparison to the immediate surroundings, higher Land Surface Temperature (LST) values of a few degrees Celsius were reported within the study landfill site [24]. They developed an analytical framework for screening illegal dump sites using nighttime light from Suomi VIIRS satellite imagery as a proxy. Karimi et al. [25] combined nighttime light imagery with LST and modified soil adjusted index alongside vector layers for highways, railways and disposal sites. The nighttime satellite imagery was used to determine populated areas [25].

 doi:10.20944/preprints202207.0410.v1

Considering the approaches implemented previously, the objective of this study was to develop a method for automatically detecting a variety of plastic waste across aquatic and terrestrial environments from EO satellite data to provide a viable approach for repeatable, cost-effective, and large-scale monitoring. More specifically, this study assessed the suitability of a Sentinel-1 and -2 synergy product for plastic waste detection using a Keras implemented Sequential model to define an Artificial Neural Network (ANN); Keras is a high-level API that runs on top of TensorFlow for this Python implementation.

ANNs are mathematical models inspired by the structure and behavior of the human brain. The multilayer perceptron supervised learning approach has multiple layers with the information transferred from the input layer to the output (feed-forward), and the weights are changed until the simulated outputs are similar to the observed ones [26]. The fusion of Sentinel-1 and -2 for land cover mapping provides the land surface's combined spectral and structural characteristics, with the results often having a higher accuracy than using either of the datasets individually [27].

2. Materials and Methods

In this study, five test sites have been used to showcase the accuracy of the detection of plastics in different environments. A classifier has been developed with a pre-processing step that processes the input satellite data such that it is suitable for the stack of layers supplied to the Neural Network classifier. Then, a post Neural Network Decision Tree is applied to refine the generated land cover classification before several accuracy measures are used to understand the classifier's ability to detect plastic waste within different scenarios.

2.1. Test sites and input satellite products

Five test sites with different types of plastic pollution are being used to demonstrate the performance of the developed classifier for automatically detecting plastic waste. The Sentinel-1 Interferometric Wide Swath (IW) Ground Range Detected High Resolution (GRDH) and Sentinel-2 Level-2A (L2A, atmospherically corrected) files used for the plastic waste detection are shown in Table 1.

Table 1. Test site locations with Sentinel-1 IW GRDH and Sentinel-2 Level 2A files as date/time and (for Sentinel-2) tile.

Test Site (co-ordinates)	Sentinel-1 IW GRDH	Sentinel-2 L2A
Višegrad Dam (43°45'35.62"N 19°17'15.68"E)	S1A 20210302T163318	S2A 20210302T09303 T34TCP*
Solo River Mouth (6°50'57.89"S 112°34'33.44"E)	S1A 20210218T220906 & 20210218T220931**	S2A 20210227T023641 T49MFN
Srinagar Landfill (34° 7'28.81"N 74°47'11.60"E)	S1A 20211031T005910	S2A 20211029T053941 T43SDT
Tyre Graveyard (29°15'24.42"N 47°40'22.96"E)	S1A 20201228T024734 & 20201228T024709**	S2A 20201226T073321 T38RQT
Almería Greenhouses (36°43'6.72"N 2°45'12.82"W)	S1A 20210408T061050	S2A 20210505T105031 T30SWF

* Processed from Level 1C to Level 2A as there were issues using the online Level 2 file

**Two Sentinel-1 files merged to cover the area of interest for the test site fully

The Sentinel-2 files are from 2021, so they have a relatively consistent processing version between themselves and the training data. Version 2.09 became active on 04 February 2020 with improvements in the NO DATA masking, then version 3.00 on 30 March 2021

 doi:10.20944/preprints202207.0410.v1

had improved geometry and masks. There was a major upgrade to version 4.0 on 25 January 2022, when the format and radiometry changed [28]. There will be a reprocessing activity in the future, so all files have consistent processing.

Sentinel-1B suffered an anomaly on 23 December 2021, so utilizing data before that date offered the opportunity to match either the Sentinel-1A or B missions. However, as shown in Table 1, Sentinel-1 was chosen in all cases. Most of the Sentinel-1 files are version 3.31, with the Srinagar Landfill file being version 3.40 [29], which is not significantly different and is not expected to affect the results.

2.1.2. Višegrad Dam, Bosnia-Herzegovina

The Drina River and its tributaries, located on the border between Bosnia and Serbia, filled with trash when weeks of wet winter weather pulled plastic bottles, rusty barrels, used tires, old furniture, and other rubbish into the water [30]. This trash built up at the Višegrad Dam, piling up faster than the authorities could clear it out, so it was detectable from space in March 2021.

2.1.2. Solo River Mouth, Indonesia

In 2020 it was reported that the Solo River in East Java, Indonesia, was polluted by plastic waste. In the dry season, rubbish covers the surface of the river, making it difficult for fishers to go to sea, while in the rainy season, trash drifts into the sea until it ends up on the beaches in Bali [31].

2.1.3. Srinagar Landfill, India

In 2021, the overflowing landfill site in Srinagar, the capital of Indian-administered Kashmir, was reported to pose a health risk to residents and damage the region's fragile ecosystem [32].

2.1.4. Tyre Graveyard, Kuwait

Tens of millions of tyres have been held in pits within a graveyard in the Arhiya area, five kilometers south of the city of Jahra [33]. There have been several fires, posing both an environmental and health hazard, so in 2021 the Kuwait government started recycling them.

2.1.5. Almería Greenhouses, Spain

The economy of Almería is dependent on agricultural products, with greenhouses constructed from plastic sheeting producing tons of fruits and vegetables alongside plastic waste. Polyethylene is preferred because of its affordability, flexibility, and ease of manufacturing [34], with the plastics being transparent or translucent with vegetation below. Several papers have focused on detecting the greenhouses themselves, e.g. [35–37], while this paper also focuses on the plastic waste between the greenhouses and in abandoned areas.

2.2. Classifier Development

All Sentinel files were downloaded through the Copernicus Open Access Hub (https://scihub.copernicus.eu/) and processed using the European Space Agency's (ESA) open-source Sentinel Application Platform (SNAP) [38] version 7.0.

2.2.1. Pre-Processing

Sentinel-1 Level-1 IW GRDH VV polarized data was converted to backscatter values using SNAP through: (i) the application of an orbit file to correct for orbital error; (ii) radiometric correction using a *Gamma0* coefficient calibration; (iii) Range-Doppler terrain correction through orthorectification against Shuttle Radar Topography Mission (SRTM) 1-arc-second Digital Elevation Model (DEM) data; (iv) the application of a Lee Sigma speckle filter; and (v) conversion to decibels (dB) to produce a non-linear valued output. This workflow is a modified version of the standard SNAP pre-processing workflow to determine the radar backscatter in dB [39], but the thermal noise correction was dropped as it was found to introduce artefacts and is primarily of use for the cross-polarisation channel. The Lee Sigma filtering was included to reduce the speckle while preserving

Preprints (www.preprints.org) | NOT PEER-REVIEWED | Posted: 27 July 2022 doi:10.20944/preprints202207.0410.v1

edges [40]. The vertical single polarisation (VV) rather than cross-polarisation (VH) data was chosen because it is more sensitive to rough surface scattering [41], and its primary role in the classification process is the separation of water from land.

Sentinel-2 Level-2A data produced by ESA was used to provide bottom-of-atmosphere reflectance imagery. When Level-2A data was unavailable, Level-1C products were atmospherically corrected through the Sen2Cor v2.10 processor [42] available in SNAP.

2.2.2. Thematic Indices

A range of optical indices were calculated covering vegetation, biophysical, water and soil thematic groups to aid in the differentiation between land cover types and waste products. The setup started with those used in Page et al. [21] and was adjusted to include additional indices to support the detection of marine plastics alongside waste sites on land.

The normalized difference vegetation index (NDVI) algorithm is a measurement of photosynthetic activity and is strongly correlated with vegetation density and vitality [42]. Designed by Tucker [41], it is based on a high reflectance in the NIR by plant matter in contrast to the strong absorption by chlorophyll-a in the red wavelengths, known as the red edge. For MSI the chosen bands were band 8 (B08) for the NIR and band 4 (B04) for Red.

$$NDVI = \frac{(NIR - Red)}{(NIR + Red)} \quad (1)$$

The soil adjusted vegetation index (SAVI) provides a hybrid between ratio-based and perpendicular indices. It is based on simple radiative transfer and a more coherent theoretical background than other vegetation indices. Developed by Huete [43], it is necessary to use a correction value that varies from 0 for very high vegetation cover to 1 for very low. For use across various land cover types, an intermediate correction value (L) of 0.5 has been used in this instance.

$$SAVI = (1 * L)\frac{(NIR - Red)}{(NIR + Red + L)} \quad (2)$$

The second normalized difference water index (NDWI2) was developed by McFeeters [44] to detect surface waters in wetlands and to allow the measurement of the extent of surface water. The index has reduced errors in separating tyres and plastic from water-dominated pixels. Previous work demonstrated more consistent values for all target land cover classes for NDWI2 compared to its predecessor, NDWI [21], MSI band 3 (B03) was used for Green.

$$NDWI2 = \frac{(Green - Red)}{(Green + Red)} \quad (3)$$

The Road Mask is based on the approach defined by Fisser [45], which includes the following criteria:

- Visible bands (B02, B03 and B04) > 0.04 to avoid building shadows
- Green/Red ratio (B03/B04) < 0.15 to avoid industry, greenhouses and other surfaces of very high reflectance
- Blue (B02) < 0.4 to be less strict with blue as we target it
- NDVI < 0.7 to avoid vegetation but keep in mind mixed pixels
- NDWI < 0.001 to avoid water
- Normalised Difference Snow Index (NDSI) < 0.0001 to avoid snow
- 0.05 > SWIR (B11) < 0.55

 doi:10.20944/preprints202207.0410.v1

The Normalised Difference Build-Up Index (NDBI) developed by Zha et al. [46] was initially applied to Landsat Thematic Mapper (TM) imagery, with MSI B11 used as the SWIR band.

$$NDBI = \frac{(SWIR - NIR)}{(SWIR + NIR)} \quad (4)$$

2.2.3. Improved Shadow Masking

Zhou et al. [47] an approach, see Equation 5, to mask cloud shadows in WorldView-3 data in an urban context using the red, green and blue bands. The algorithm was applied to MSI by using the B04, B03 and B02 bands that were first converted into the YCbCr colour space and then the Improved Shadow Index (ISI) was calculated.

$$ISI = \frac{SI + (1 - NIR)}{SI + (1 + NIR)} \quad (5)$$

$$SI = \frac{Cb - Y}{Cb + Y} \quad (6)$$

Where Y is the luma component and Cb is the blue-difference chroma component of the Tsai [48] YCbCr model.

To further support the application in aquatic and terrestrial environments as opposed to the original purely urban context, the resulting ISI layer was adjusted using NDWI2; otherwise, all open water pixels were flagged as shadow. Also, to account for terrain shadowing, which can also cause misclassification, the terrain slope was calculated from the DEM, SRTM accessed during the Sentinel-1 processing, and high slope pixels were added to the ISI to create a raster layer termed the shadow mask. Figure 1 shows an example of the developed shadow mask applied to an area with clouds. The ISI was used as a layer in the ANN, while the shadow mask was used in the post-processing decision tree that reassigns pixels that the ANN has misclassified.

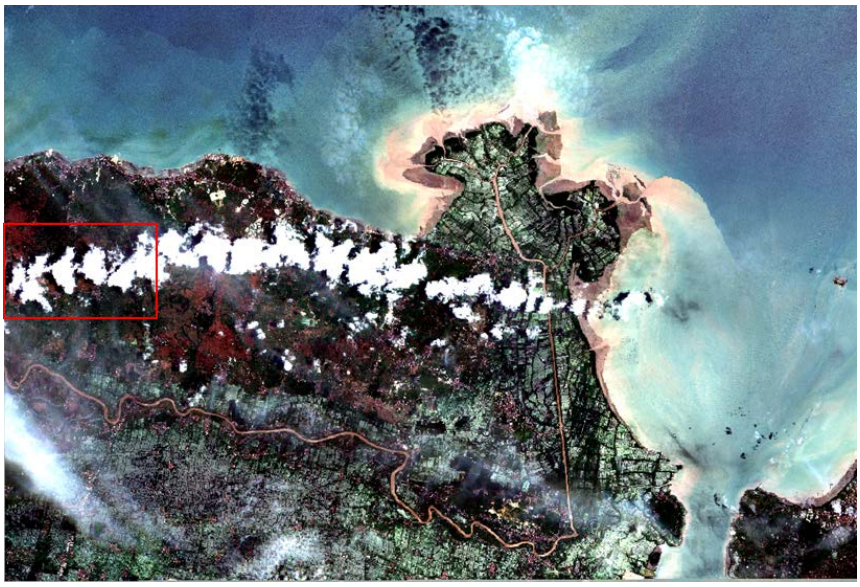

 doi:10.20944/preprints202207.0410.v1

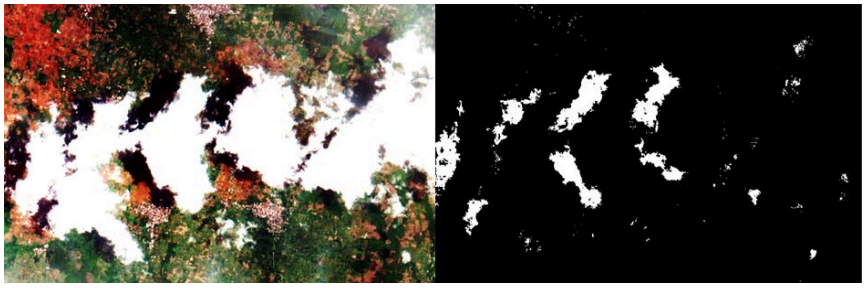

Figure 1. Full Sentinel-2 tile processed for the Solo River, Indonesia, as the pseudo-true colour image (bands B04, B03 and B02 as red, green, and blue) at the top, with a zoomed-in (see red box) comparison of pseudo-true colour to the pixels that have been identified using the shadow index for a subset.

2.2.4. Neural Network

All thematic indices were stacked into one file alongside a subset of Sentinel-2 MultiSpectral Instrument (MSI) bands, and the Sentinel-1 Gamma0 VV data. The resulting stack consists of 17 layers (Table 2). Different Sentinel-2 bands have different spatial resolutions in the original Sentinel datasets, so the coarser spatial resolution band were resampled to 10 m. For Sentinel-2, this occurs just before inclusion in the stack using the SNAP raster resampling tool, and for Sentinel-1 it is included as part of the terrain correction.

Table 2. Layers within the classification stack, including the spatial resolution and MultiSpectral Instrument (MSI) band and central wavelength for the Sentinel-2 reflectance bands.

Layer Number	MSI Band Number and Central Wavelength (nm)	Description	Original Spatial Resolution (m)
1	B02 (490)	Blue	10
2	B03 (560)	Green	10
3	B04 (665)	Red	10
4	B05 (705)	Red Edge	20
5	B06 (740)	Red Edge	20
6	B07 (783)	Red Edge	20
7	B08 (842)	NIR	10
8	B08A (865)	Red Edge	20
9	B11 (1 610)	SWIR	20
10	B12 (1 190)	SWIR	20
11		NDVI	10
12		SAVI	10
13		NDWI2	10
14		Road Mask	10
15		NDBI	10
16		ISI	10
17		Gamma0 VV	5*20

An augmented land cover classification is the desired output of the ANN classifier, which is separated into nine classes (see Table 3). These classes are adapted from the CORINE land cover mapping scheme [49], a consistent classification system developed for application in Europe. The classes were modified by adding plastics as an additional Level 2 class and then the different types of plastics (where plural the paper refers to the four Level 3 classes together).

Preprints (www.preprints.org) | NOT PEER-REVIEWED | Posted: 27 July 2022 doi:10.20944/preprints202207.0410.v1

Table 3. Classification of the land cover types through a tiered approach following CORINE, with an additional Level 2 class for plastics.

Level 1		Level 2		Level 3	
1.	Water	1.1.	Clear Water		
		1.2.	Algal Blooms		
		1.3.	Aqueous Deposits		
2.	Land	2.1.	Non-Photosynthetic		
		2.2.	Green Vegetation	2.2.1.	Woodland
				2.2.2.	Grassland
		2.3.	Urban	2.3.1.	Industrial
				2.3.2.	Artificial Surfaces
		2.4.	Plastics	2.4.1	Tyres
				2.4.2	Plastic
				2.4.3	Greenhouses
				2.4.4	Waste sites

Separate plastic, tyres, waste site and greenhouses classes were used to minimize confusion in classifying these different types of plastics. Misclassification occurs because of spectral similarities between the classes. Also, waste often co-exists, i.e., tyre waste is covered in plastic sheeting, and plastic sheeting is weighed down with tyres. Also, the waste sites class is confused with bare ground as soil versus waste mixture per pixel varies across the sites.

The training/validation dataset used Sentinel-1 and -2 satellite imagery collected over a global set of test sites with training pixels manually identified using a combination of the high spatial resolution satellite imagery within Google Earth and the Sentinel-2 RGB colour composite; see Figure 2. Where the locations of the plastics could not be reliably identified, these land cover classes were not digitized, and the background land cover classes were only digitized so as not to reduce the accuracy of the overall dataset.

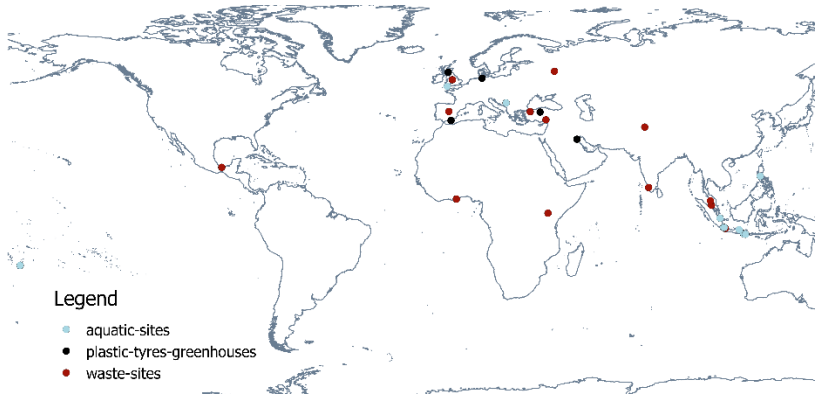

Figure 2. Locations and focus for the manually digitized training/validation dataset.

For each target class, multiple homogeneous training pixels were taken across the different sites through the digitizing of polygons that resulted in the pixel numbers shown in Table 4. As the original plastics classes of interest have low numbers of pixels, such that they are from 0% to 0.3% of the total pixels to within 1dp, the training/validation dataset has a class imbalance. Therefore, a re-weighting was applied to reduce the number of pixels for the classes with high numbers, such as clear water and clouds, and increased the

 doi:10.20944/preprints202207.0410.v1

number of pixels for classes with low numbers through duplication. The result is that this approach has reduced the class imbalance, although it remains and should be accounted for when assessing performance.

Table 4. Training sample distribution amongst the classes.

Class	Original Number of Pixels	Original Percentage	Updated Number of Pixels	Updated Percentage
Clear Water	810 210	65.4%	587 792	47.5%
Algal Blooms	10 184	0.8%	27 773	2.2%
Aqueous Deposits	37 924	3.1%	47 191	3.8%
Bare Ground	34 307	2.8%	44 659	3.6%
Murrum Soil	56	0.0%	20 683	1.7%
Sand	9 097	0.7%	27 012	2.2%
Grassland	11 513	0.9%	28 703	2.3%
Shrubland	10 341	0.8%	27 882	2.3%
Forest	31 502	2.5%	42 695	3.4%
Cropland	7 939	0.6%	26 201	2.1%
Buildings	7 038	0.6%	25 570	2.1%
Artificial Surfaces	7 519	0.6%	25907	2.1%
Cloud	247 323	20.0%	193 771	15.6%
Shadow	7 387	0.6%	25 815	2.1%
Plastic	667	0.0%	21 111	1.7%
Tyres	351	0.0%	20 889	1.7%
Greenhouses	4 163	0.3%	23 558	1.9%
Waste Sites	1 143	0.1%	21 444	1.7%
Total number after adjustment	1 238 656 pixels split into 928 992 training pixels and 309 664 validation pixels			

Different models were tested to investigate the bands that could be used and their relative contribution: Linear Regression, Random Forest and ANN. As it was difficult to understand the different input layer contributions to the ANN out, the relative importance was tested using the two other types of models. Figure 3 shows the resulting layer importance graphs for applying Linear Regression and Random Forest models generated using the permutation importance function in the sklearn Python module; it was not possible to apply this function to the ANN due to its model structure that was not compatible. The graphs are log-scaled as the single bands for the Linear Regression model contribute significantly more than the SAR-derived roughness. In contrast, all layers except for the Road Mask significantly contribute to the Random Forest model.

Preprints (www.preprints.org) | NOT PEER-REVIEWED | Posted: 27 July 2022 doi:10.20944/preprints202207.0410.v1

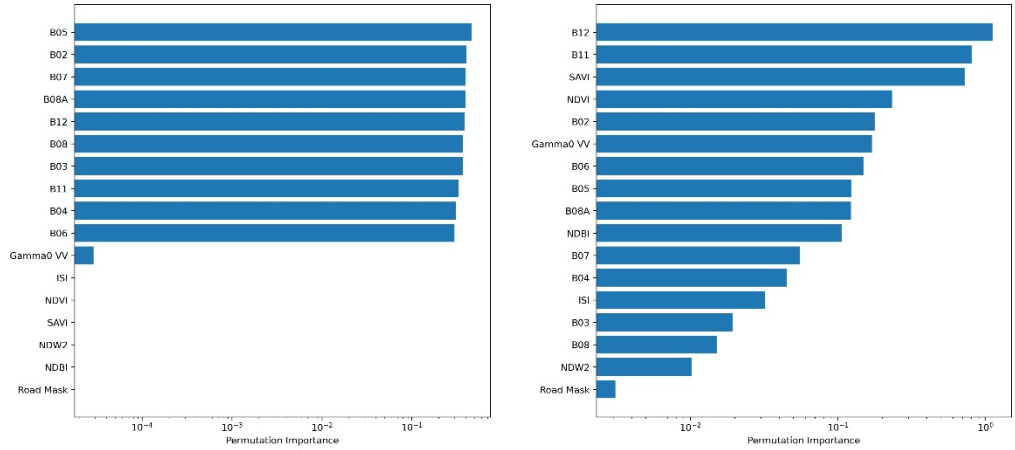

Figure 3. Linear Regression (left) and Random Forest (right) layer importance.

The ANN model, shown in Figure 4 (left), was generated using a Sequential model that creates a deep learning model by adding layers; sequential patterns are important because they can be exploited to improve the prediction accuracy of classifiers. The layers include:

- Flatten is used to flatten all its input into a single dimension.
- Dense implements a regular, deeply connected neural network layer that receives inputs from all neurons in the previous layer and applies a matrix-vector multiplication.
- Dropout reduces the training dataset size so that overtraining does not occur.

The model training used the KerasTuner [50] to iteratively perform testing until the optimal model setup was achieved in terms of the overall accuracy achieved with the resulting Loss function shown in Figure 4 (right) used to diagnose the behavior of the model. In this case, as should occur, the training and validation plots of loss and accuracy have converged over successive epochs.

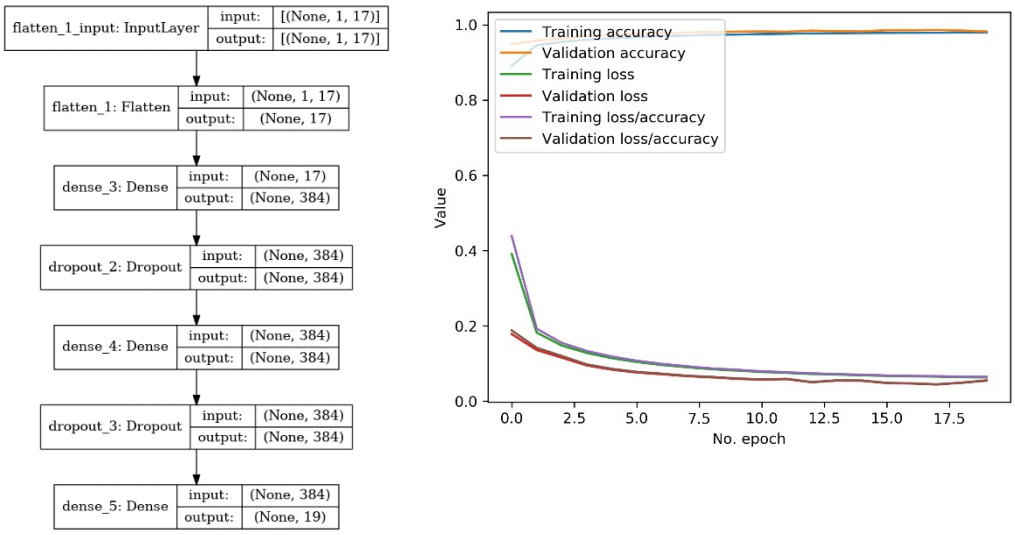

Figure 4. Artificial Neural Network model (left) and training loss plot (right) generated during the training process.

Preprints (www.preprints.org) | NOT PEER-REVIEWED | Posted: 27 July 2022 doi:10.20944/preprints202207.0410.v1

Figure 5 shows the confusion matrices generated during the training to indicate the ANN and RF performance across all land cover classes. For the ANN (Figure 5 left), there is some misclassification, but overall, most validation pixels fall on the prime diagonal; a value of 1.0 indicates all validation pixels were assigned to the same class they were digitized according to. A similar result is seen for the Random Forest model (Figure 5 right) but with increased confusion between bare ground and tyres.

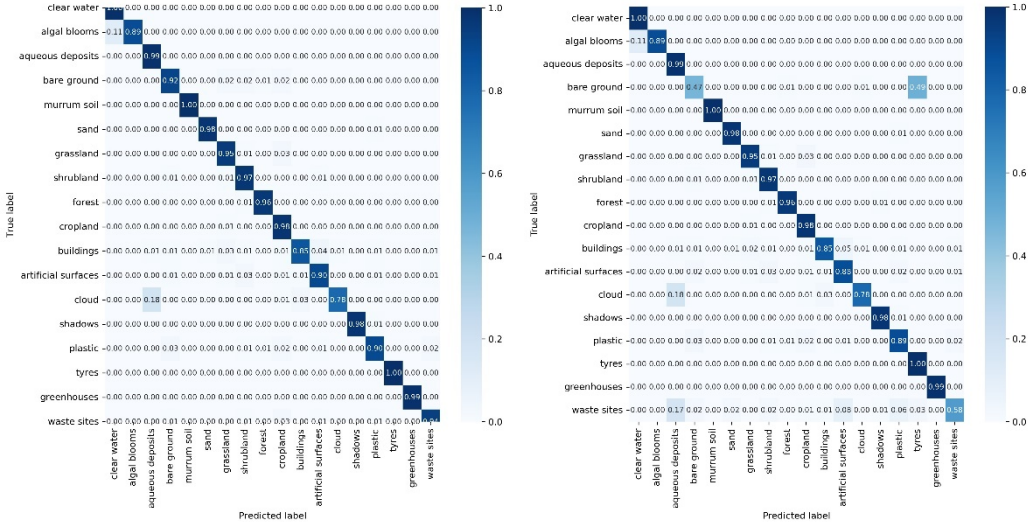

Figure 5. Neural Network model (left) and Random Forest (right) confusion matrix generated during the training process.

2.2.5. Post Neural Network Decision Tree

The post-ANN decision tree, see Figure 6, was used for reclassification. It was discovered through testing the performance across multiple sites that the ANN could not fully capture a radiometric interpretation of the surface and is also not designed to accept categorical layers.

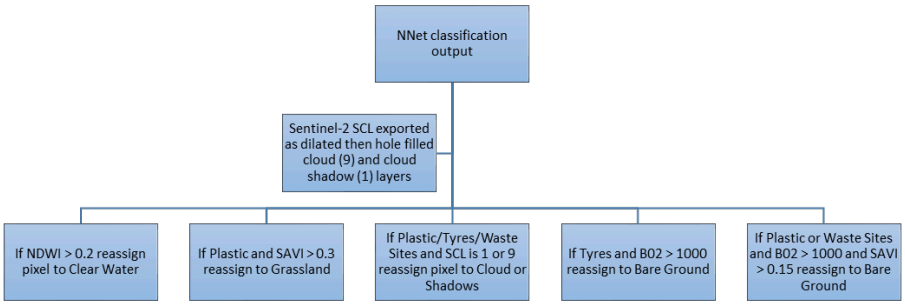

Figure 6. Post-Artificial Neural Network decision tree.

The Sentinel-2 Scene Classification Layer (SCL) was extracted from the Sentinel-2 L2A file and resampled to 10 m resolution; pixels classified as cloud (value of 9) and cloud shadow (value of 1) were used. Then the Python multidimensional image processing library (scipy.ndimage) was then applied so the pixel values were extracted as dilated and hole-filled binary layers. This meant that both cloud edges and cloud shadow edges could be captured, which was essential as both can end up misclassified as plastics. Also, the previously calculated shadow mask (Section 2.2.3) was used to further exclude pixels influenced by shadow from being classified as plastics and plastic/tyre/waste pixels were

Preprints (www.preprints.org) | NOT PEER-REVIEWED | Posted: 27 July 2022 doi:10.20944/preprints202207.0410.v1

reclassified where they had a high NDWI value, high SAVI value or high B02 reflectance, as these were found to be frequent misclassifications.

Figure 7 shows the classification results' differences before and after the post-network decision tree. The cloud shadows (grey) have been filled in as the pixels within these are likely to be incorrect. In addition, the number of plastic (red) pixels have been reduced in the top right to what mixed cloud pixels exist. Incorrectly, bare ground cultivated pixels are classified as waste sites (lilac) as the current bare ground training data isn't sufficiently capturing the soil's spectral properties. In the RGB pseudo-true colour composite (Figure 1), the soil appears red, which might alternatively indicate the atmospheric correction is erroneous due to the high aerosol load.

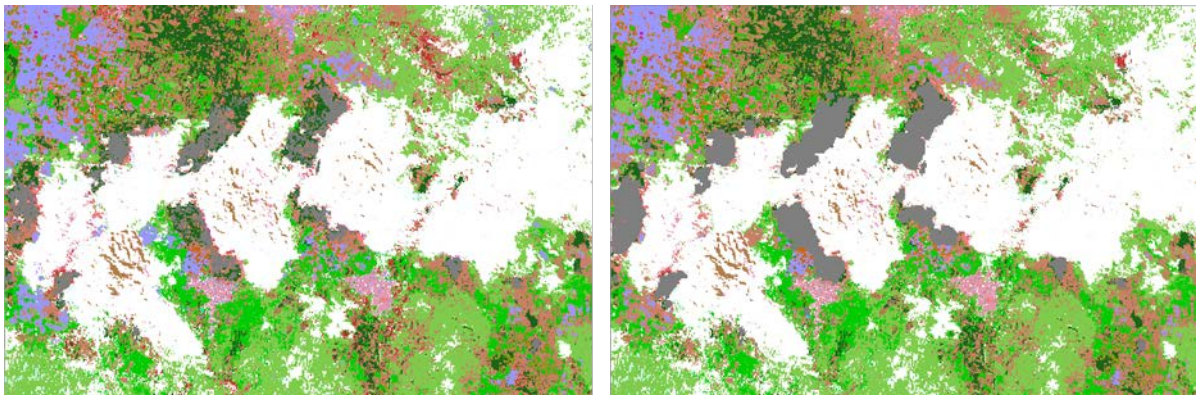

Figure 7. Comparison of the classification results before and after the post-network decision tree for the subset of the Solo River location shown in Figure 1.

2.3. Accuracy Assessment Methodology

The correctness of a classification can be evaluated by computing the number of correctly recognized class examples (True Positives), the number of correctly recognized examples that do not belong to the class (True Negatives), and examples that either were incorrectly assigned to the class (False Positives) or that were not recognized as class examples (False Negatives) [51]. These four counts constitute a confusion matrix, from which Precision and Recall are calculated and commonly used to evaluate classification performance [52]:

$$Precision = \frac{TP}{(TP + FP)} \tag{7}$$

$$Recall = \frac{TP}{(TP + FN)} \tag{8}$$

Precision (Equation 7) quantifies the proportion of the predicted positives that were truly positive, while Recall (Equation 8) is a measure of the proportion of actual positives which were classified correctly. The average of all accuracy values yielded the aggregate average Precision.

As accuracy is not a good metric to use when there is a class imbalance, which we have, the F1-score that assesses the Precision-Recall trade-off has also been calculated [52]; see Equation 9. The F1-score ranges from zero to one, with a high value indicating high classification performance.

$$F1 - score = \frac{2 * Precision * Recall}{Precision + Recall} \tag{9}$$

Also, Cohen's KAPPA coefficient is a statistical measure of agreement that provides a more robust result than percentage agreement calculations [53]. In the equations below,

Preprints (www.preprints.org) | NOT PEER-REVIEWED | Posted: 27 July 2022 doi:10.20944/preprints202207.0410.v1

p_o is the observed agreement (percentage of instances classified correctly from the error matrix), and p_e is the expected agreement. The overall expected agreement is calculated using Equation 10, where the expected agreement is calculated for each class, and then these are added together and divided by the total number of pixels.

$$KAPPA = \frac{(p_o - p_e)}{(1 + p_e)} \tag{10}$$

$$p_e = \frac{(expected_{class1} + expected_{class2} + \cdots)}{N} \tag{11}$$

$$expected_{class1} = \frac{(actual_{class1} * estimated_{class1})}{N} \tag{12}$$

3. Results

This section showcases the accuracy statistics extracted during the training process and the classification results for the Test sites.

3.1. Accuracy Statistics of the Training Process

The accuracy statistics for the training process are shown in Table 5, with the Precision and Recall alongside F-score calculated for each class. All the Precision values except Aqueous Deposits are high, greater than 0.8, equating to the classifier being correct more than 80% of the time. In addition, all the Recall values are also high; the classifier can capture most of the positive predictions. In addition, the F1-scores are high except for Aqueous Deposits, i.e., both Precision and Recall are high.

In addition, the average Precision and KAPPA coefficient were calculated for the aggregate of all the classes, with both also presenting high values of 95% and 0.86. A KAPPA value of greater than 0.81 is classified as "Almost Prefect" [54].

Table 5. ANN accuracy statistics generated during the training process.

Class	Precision	Recall	F1-score
Clear Water	0.99	1.00	1.00
Algal Blooms	1.00	0.89	0.94
Aqueous Deposits	0.57	0.89	0.72
Bare Ground	0.95	0.92	0.93
Murrum Soil	1.00	1.00	1.00
Sand	0.99	0.98	0.98
Grassland	0.92	0.95	0.94
Shrubland	0.90	0.97	0.93
Forest	0.96	0.96	0.96
Cropland	0.84	0.98	0.91
Buildings	0.78	0.85	0.82
Artificial Surfaces	0.91	0.90	0.91
Cloud	0.99	0.78	0.88
Shadow	0.99	0.98	0.98
Plastic	0.91	0.90	0.90
Tyres	1.00	1.00	1.00
Greenhouses	0.99	0.99	0.99
Waste Sites	0.95	0.94	0.94
Aggregate average Precision		0.95	
KAPPA coefficient		0.86	

Preprints (www.preprints.org) | NOT PEER-REVIEWED | Posted: 27 July 2022 doi:10.20944/preprints202207.0410.v1

Figure 8 shows examples of layer values extracted from the test sites for the Sentinel-2 bands 12 and 11 in the SWIR, SAVI and NDVI vegetation indices, Sentinel-2 band 2 (blue) and the Sentinel-1 Gamma0 VV layers. In terms of importance, these are the top six layers identified when the Random Forest model was executed on the training dataset; see Figure 2 (right), and the increased darkness indicates a greater number of pixels as indicated by the legend. For the plastics categories, there is a separation, but the layer pixel ranges do overlap with non-plastic classes. So, for example, greenhouses exist with the range of pixel values seen within clouds.

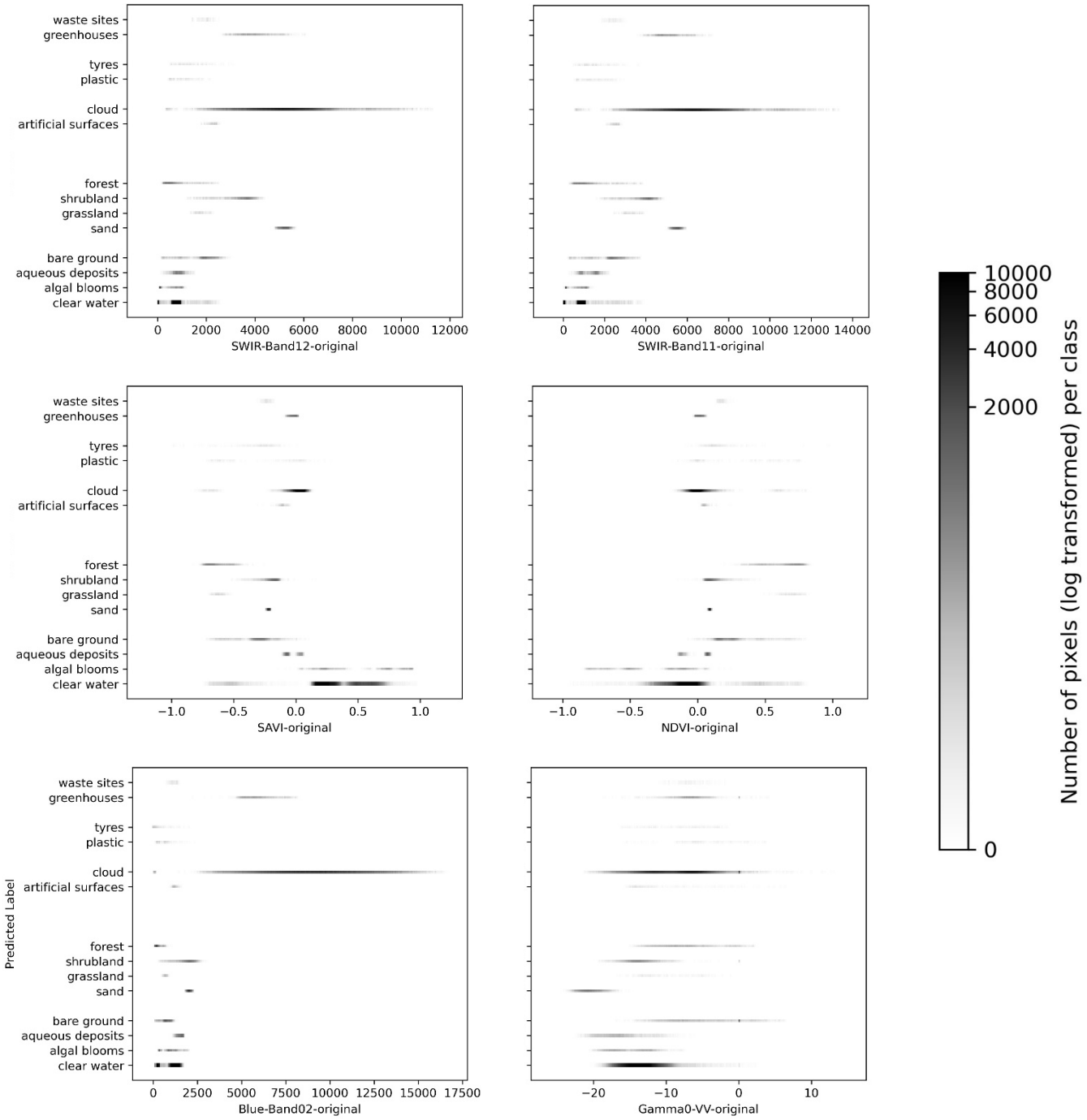

Figure 8. Horizontal density plots show the distribution of the values for the manually labelled pixels in each land cover class for the five test sites, for the Sentinel-2 bands 12 and 11 in the SWIR, SAVI and NDVI vegetation indices, Sentinel-2 band 2 (blue) and the Sentinel-1 Gamma0 VV layers.

 doi:10.20944/preprints202207.0410.v1

3.2. Application to the Test Sites

Figures 9 and 10 show the results of the classifier applied to the five test sites, which indicates the performance for different types of plastic and with varying land cover backgrounds.

For the Višegrad Dam river accumulation, Figure 9 (top), and Solo mouth test site, Figure 9 (bottom), it is predominately plastic (red) that is being detected. For the river mouth example, there are thin cloud and cloud shadow pixels, and some are classified as artificial surfaces where the cloud masking has not removed all cloud pixels.

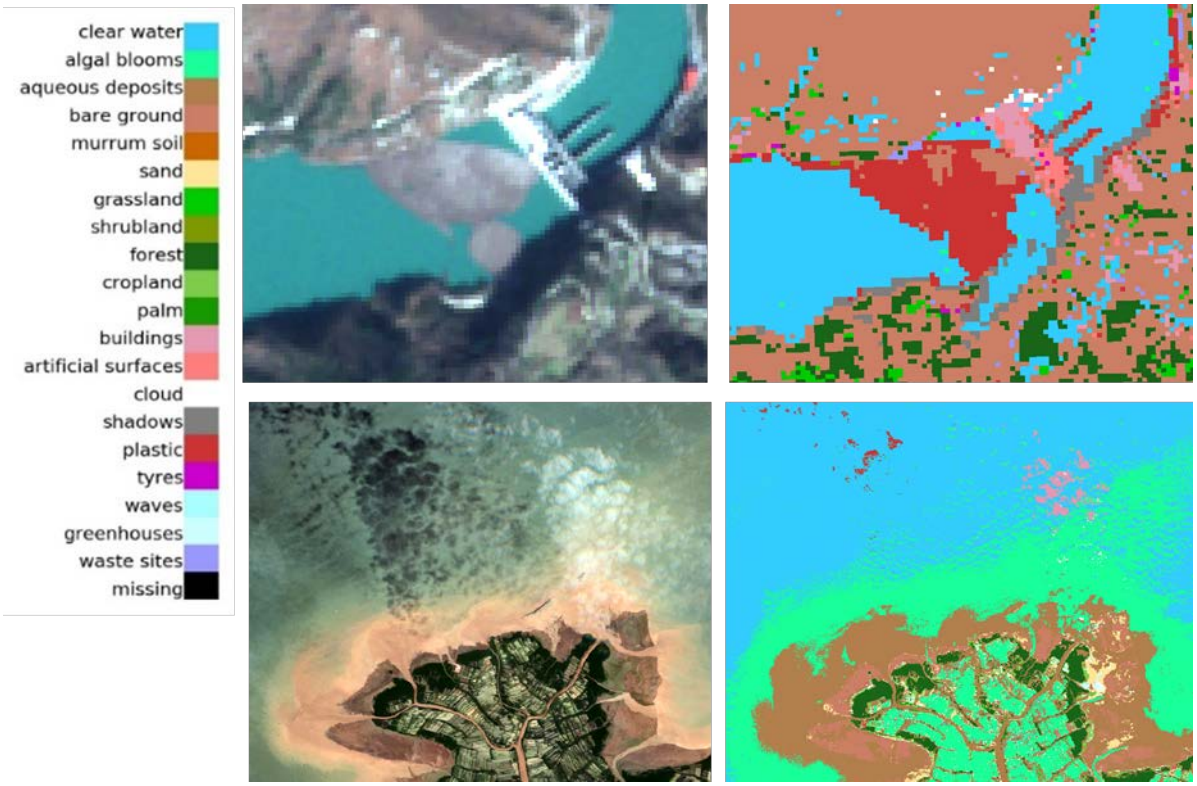

Figure 9. Comparison of the Sentinel-2 pseudo-true colour image (bands B04, B03 and B02 as red, green, and blue) on the left and classification output for the riverine/marine sites on the right. From top to bottom, the subsetted areas are the Višegrad Dam with plastic (red) detected for the accumulation behind the dam and the Solo River Mouth with plastic (red) pixels in the sea offshore.

A mixture of plastic (red) and waste sites (lilac) pixels are being classified for the Srinagar Landfill in Figure 10 (top). For the Almería province of Spain, on the coast, Figure 10 (middle) shows an area dominated by greenhouses, with the greenhouses themselves being classified according to this category (light blue) but also as clouds (white) and buildings (pale pink). In between the greenhouses, there are areas classified as plastic (red) that predominately coincide with the storage of water within pools lined with black plastic. The third site, Figure 10 (bottom) is the tyre graveyard in Kuwait, with the tyre pits predominately classified correctly (cerise), although there are also pixels classified as artificial surfaces (bright pink).

Preprints (www.preprints.org) | NOT PEER-REVIEWED | Posted: 27 July 2022 doi:10.20944/preprints202207.0410.v1

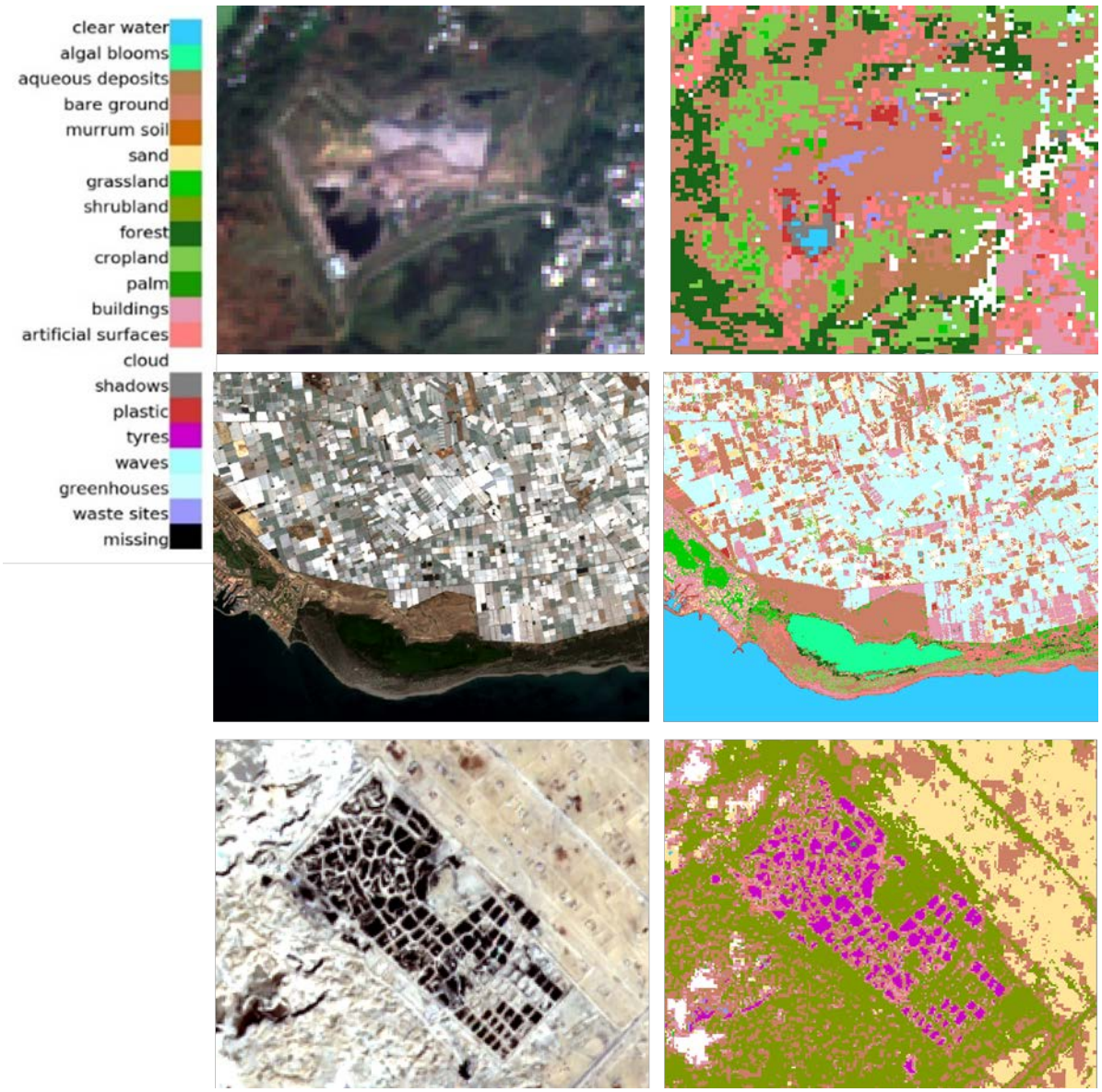

Figure 10. Comparison of the Sentinel-2 pseudo-true colour image (bands B04, B03 and B02 as red, green, and blue) on the left and classification output for the terrestrial locations on the right. From top to bottom, the subsetted areas are the Srinagar Landfill with plastic (red) and waste (lilac) detected within the boundaries of the site, the tyre graveyard in Kuwait with the tyre piles classified as tyres (cerise), and Almería with greenhouses (light blue) detected alongside plastic (red).

4. Discussion

The developed classifier includes pre-processing, ANN and decision tree steps that can accurately classify different forms of waste plastic and separate them when they are present in their distinct environments. However, it will also generate false positives and negatives due to similar spectral signatures and where plastic waste is in low concentrations compared to the background signal. The decision tree step can be tuned depending on whether the user wishes the results to be conservative or relaxed. Currently, a conservative approach has been adopted because when time-series datasets are automatically processed, a build-up of false positives becomes distracting to users when they look at composite outputs.

The training/validation dataset has been built up carefully through manual digitizing, and finding sufficient plastics pixels has been challenging despite several sites having been identified. Kruse et al. [22] faced similar issues as this research because the visual

 doi:10.20944/preprints202207.0410.v1

inspection of such waste, even using higher-resolution imagery, does not allow human labelers to delineate boundaries between bare earth and waste reliably. So, these two classification categories overlap.

The current remote sensing approach primarily uses spectral information. However, as part of the post-processing, when time-series datasets are classified, there is an optional additional step (not shown) that clusters waste pixels and remove small clusters (< 5 pixels). This extra step allows the approach to focus the output on more significant accumulations of waste and remove individual erroneous miss-classifications. Other features, such as textural or spatial features, have not been the focus because of the spatial resolution of the Copernicus data but may be considered if data from higher-resolution satellite data are included.

5. Conclusions

The developed classifier has proven to be helpful in several applications, including detecting waste plastics in aquatic and terrestrial environments. As Sentinel-1 acquisitions do not coincide with Sentinel-2 tile acquisitions, the combined use of the two missions is not ideally suited to detect plastic floating on water where objects will move over a few days. However, Sentinel-1 improves the overall result when the classifier is applied in terrestrial environments or when there are relatively stationary floating accumulations.

Funding: This research and the APC were primarily funded by the European Space Agency through the CLS-led MARLISAT project, contract number 4000131481/20/NL/GLC. In addition, the RisikoTek Pte Ltd-led Space Detective project funded by the Singapore Government, grant number 2010JVVZ, supported gathering additional training data and testing.

Data Availability Statement: The training data is being submitted to Ocean Scan (https://www.oceanscan.org/), with an initial dataset having the DOI: 10.5281/zenodo.6245460.

Acknowledgements: Dr Ashley Smith and Sarah Lappin are acknowledged for their work supporting the development of the classification approach within MARLISAT.

Conflicts of Interest: The author declares no conflict of interest.

References

1. Royer, S.-J.; Ferrón, S.; Wilson, S.T.; Karl, D.M. Production of Methane and Ethylene from Plastic in the Environment. *PLoS ONE* **2018**, *13*, e0200574, doi:10.1371/journal.pone.0200574.
2. The World's Plastic Pollution Crisis Explained. Available online: https://www.nationalgeographic.com/environment/article/plastic-pollution (accessed on 1 May 2022).
3. Elhacham, E.; Ben-Uri, L.; Grozovski, J.; Bar-On, Y.M.; Milo, R. Global Human-Made Mass Exceeds All Living Biomass. *Nature* **2020**, *588*, 442–444, doi:10.1038/s41586-020-3010-5.
4. Dumbili, E.; Henderson, L. The Challenge of Plastic Pollution in Nigeria. In *Plastic Waste and Recycling*; Elsevier, 2020; pp. 569–583 ISBN 978-0-12-817880-5.
5. Fly-Tipping Statistics for England, 2020 to 2021 Available online: https://www.gov.uk/government/statistics/fly-tipping-in-england/fly-tipping-statistics-for-england-2020-to-2021 (accessed on 1 May 2022).
6. Waste Disguised as Hay Bales at Turnhouse Farm in Edinburgh. Available online: https://www.bbc.co.uk/news/uk-scotland-edinburgh-east-fife-29567276 (accessed on 20 March 2020).
7. Household Waste Disguised as Hay Bales Dumped in Essex. Available online: https://www.bbc.co.uk/news/uk-england-essex-22135870 (accessed on 20 March 2020).
8. Briassoulis, D.; Babou, E.; Hiskakis, M.; Scarascia, G.; Picuno, P.; Guarde, D.; Dejean, C. Review, Mapping and Analysis of the Agricultural Plastic Waste Generation and Consolidation in Europe. *Waste Manag Res* **2013**, *31*, 1262–1278, doi:10.1177/0734242X13507968.
9. European Commission Waste Framework Directive Available online: https://environment.ec.europa.eu/topics/waste-and-recycling/waste-framework-directive_en (accessed on 27 June 2022).
10. Quinlan, B.L.; Foschi, P.G. Identification of Waste Tires Using High-Resolution Multispectral Satellite Imagery. *photogramm eng remote sensing* **2012**, *78*, 463–471, doi:10.14358/PERS.78.5.463.
11. World Business Council for Sustainable Development End-of-Life Tires Available online: https://www.wbcsd.org/Sector-Projects/Tire-Industry-Project/News/End-of-Life-Tires (accessed on 27 June 2022).
12. Enfrin, M.; Dumée, L.F.; Lee, J. Nano/Microplastics in Water and Wastewater Treatment Processes – Origin, Impact and Potential Solutions. *Water Research* **2019**, *161*, 621–638, doi:10.1016/j.watres.2019.06.049.
13. Jambeck, J.R.; Geyer, R.; Wilcox, C.; Siegler, T.R.; Perryman, M.; Andrady, A.; Narayan, R.; Law, K.L. Plastic Waste Inputs from Land into the Ocean. *Science* **2015**, *347*, 768–771, doi:10.1126/science.1260352.
14. Biermann, L.; Clewley, D.; Martinez-Vicente, V.; Topouzelis, K. Finding Plastic Patches in Coastal Waters Using Optical Satellite Data. *Sci Rep* **2020**, *10*, 5364, doi:10.1038/s41598-020-62298-z.
15. Themistocleous, K.; Papoutsa, C.; Michaelides, S.; Hadjimitsis, D. Investigating Detection of Floating Plastic Litter from Space Using Sentinel-2 Imagery. *Remote Sensing* **2020**, *12*, 2648, doi:10.3390/rs12162648.
16. Sivadas, S.K.; Mishra, P.; Kaviarasan, T.; Sambandam, M.; Dhineka, K.; Murthy, M.V.R.; Nayak, S.; Sivyer, D.; Hoehn, D. Litter and Plastic Monitoring in the Indian Marine Environment: A Review of Current Research, Policies, Waste Management, and a Roadmap for Multidisciplinary Action. *Marine Pollution Bulletin* **2022**, *176*, 113424, doi:10.1016/j.marpolbul.2022.113424.
17. Hasituya; Chen, Z.; Wang, L.; Wu, W.; Jiang, Z.; Li, H. Monitoring Plastic-Mulched Farmland by Landsat-8 OLI Imagery Using Spectral and Textural Features. *Remote Sensing* **2016**, *8*, 353, doi:10.3390/rs8040353.
18. Levin, N.; Lugassi, R.; Ramon, U.; Braun, O.; Ben-Dor, E. Remote Sensing as a Tool for Monitoring Plasticulture in Agricultural Landscapes. *International Journal of Remote Sensing* **2007**, *28*, 183–202, doi:10.1080/01431160600658156.
19. Goddijn-Murphy, L.; Dufaur, J. Proof of Concept for a Model of Light Reflectance of Plastics Floating on Natural Waters. *Marine Pollution Bulletin* **2018**, *135*, 1145–1157, doi:10.1016/j.marpolbul.2018.08.044.

20. Guffogg, J.A.; Blades, S.M.; Soto-Berelov, M.; Bellman, C.J.; Skidmore, A.K.; Jones, S.D. Quantifying Marine Plastic Debris in a Beach Environment Using Spectral Analysis. *Remote Sensing* **2021**, *13*, 4548, doi:10.3390/rs13224548.
21. Page, R.; Lavender, S.; Thomas, D.; Berry, K.; Stevens, S.; Haq, M.; Udugbezi, E.; Fowler, G.; Best, J.; Brockie, I. Identification of Tyre and Plastic Waste from Combined Copernicus Sentinel-1 and -2 Data. *Remote Sensing* **2020**, *12*, 2824, doi:10.3390/rs12172824.
22. Kruse, C.; Boyda, E.; Chen, S.; Karra, K.; Bou-Nahra, T.; Hammer, D.; Mathis, J.; Maddalene, T.; Jambeck, J.; Laurier, F. Satellite Monitoring of Terrestrial Plastic Waste. **2022**, doi:10.48550/ARXIV.2204.01485.
23. Gill, J.; Faisal, K.; Shaker, A.; Yan, W.Y. Detection of Waste Dumping Locations in Landfill Using Multi-Temporal Landsat Thermal Images. *Waste Manag Res* **2019**, *37*, 386–393, doi:10.1177/0734242X18821808.
24. Yan, W.Y.; Mahendrarajah, P.; Shaker, A.; Faisal, K.; Luong, R.; Al-Ahmad, M. Analysis of Multi-Temporal Landsat Satellite Images for Monitoring Land Surface Temperature of Municipal Solid Waste Disposal Sites. *Environ Monit Assess* **2014**, *186*, 8161–8173, doi:10.1007/s10661-014-3995-z.
25. Karimi, N.; Ng, K.T.W.; Richter, A. Development and Application of an Analytical Framework for Mapping Probable Illegal Dumping Sites Using Nighttime Light Imagery and Various Remote Sensing Indices. *Waste Management* **2022**, *143*, 195–205, doi:10.1016/j.wasman.2022.02.031.
26. Olaya-Marín, E.J.; Martínez-Capel, F.; Vezza, P. A Comparison of Artificial Neural Networks and Random Forests to Predict Native Fish Species Richness in Mediterranean Rivers. *Knowl. Managt. Aquatic Ecosyst.* **2013**, 07, doi:10.1051/kmae/2013052.
27. Liang, J.; Liu, D. A Local Thresholding Approach to Flood Water Delineation Using Sentinel-1 SAR Imagery. *ISPRS Journal of Photogrammetry and Remote Sensing* **2020**, *159*, 53–62, doi:10.1016/j.isprsjprs.2019.10.017.
28. ESA Sentinel-2 Processing Baseline Available online: https://sentinels.copernicus.eu/web/sentinel/technical-guides/sentinel-2-msi/processing-baseline (accessed on 18 June 2022).
29. SAR-MPC Sentinel-1 IPF Versions Available online: https://sar-mpc.eu/ipf/ (accessed on 18 June 2022).
30. Emric, E. Trash Fills Bosnia River Faster than Workers Can Pull It Out Available online: https://apnews.com/article/environment-serbia-hydroelectric-power-95866b7e3af63b9608218e89791df5d0 (accessed on 5 June 2022).
31. Kresna, M. Plastic Trash Runs down the Solo River to Pollute the Java Sea Available online: https://earthjournalism.net/stories/plastic-trash-runs-down-the-solo-river-to-pollute-the-java-sea (accessed on 5 June 2022).
32. Batool, M. Strategy for Solid Waste Management in Srinagar Available online: https://www.greaterkashmir.com/todays-paper/strategy-for-solid-waste-management-in-srinagar (accessed on 5 June 2022).
33. Mukhtar, I. Kuwait Struggling to Get Rid of World's Biggest Tire Graveyard Available online: https://www.aa.com.tr/en/environment/kuwait-struggling-to-get-rid-of-world-s-biggest-tire-graveyard/2332769 (accessed on 19 June 2022).
34. Scarascia-Mugnozza, G.; Sica, C.; Russo, G. PLASTIC MATERIALS IN EUROPEAN AGRICULTURE: ACTUAL USE AND PERSPECTIVES. *J Agricult Engineer* **2012**, *42*, 15, doi:10.4081/jae.2011.28.
35. Zhou, S.; Kuester, T.; Bochow, M.; Bohn, N.; Brell, M.; Kaufmann, H. A Knowledge-Based, Validated Classifier for the Identification of Aliphatic and Aromatic Plastics by WorldView-3 Satellite Data. *Remote Sensing of Environment* **2021**, *264*, 112598, doi:10.1016/j.rse.2021.112598.
36. Feng, Q.; Niu, B.; Chen, B.; Ren, Y.; Zhu, D.; Yang, J.; Liu, J.; Ou, C.; Li, B. Mapping of Plastic Greenhouses and Mulching Films from Very High Resolution Remote Sensing Imagery Based on a Dilated and Non-Local Convolutional Neural Network. *International Journal of Applied Earth Observation and Geoinformation* **2021**, *102*, 102441, doi:10.1016/j.jag.2021.102441.

37. Zhang, P.; Du, P.; Guo, S.; Zhang, W.; Tang, P.; Chen, J.; Zheng, H. A Novel Index for Robust and Large-Scale Mapping of Plastic Greenhouse from Sentinel-2 Images. *Remote Sensing of Environment* **2022**, *276*, 113042, doi:10.1016/j.rse.2022.113042.
38. STEP: Science Toolbox Exploitation Platform. Available Online Available online: http://step.esa.int/main/toolboxes/snap/ (accessed on 20 March 2020).
39. Truckenbrodt, J.; Freemantle, T.; Williams, C.; Jones, T.; Small, D.; Dubois, C.; Thiel, C.; Rossi, C.; Syriou, A.; Giuliani, G. Towards Sentinel-1 SAR Analysis-Ready Data: A Best Practices Assessment on Preparing Backscatter Data for the Cube. *Data* **2019**, *4*, 93, doi:10.3390/data4030093.
40. Filipponi, F. Sentinel-1 GRD Preprocessing Workflow. In Proceedings of the 3rd International Electronic Conference on Remote Sensing; MDPI, June 4 2019; p. 11.
41. Joshi, N.; Baumann, M.; Ehammer, A.; Fensholt, R.; Grogan, K.; Hostert, P.; Jepsen, M.; Kuemmerle, T.; Meyfroidt, P.; Mitchard, E.; et al. A Review of the Application of Optical and Radar Remote Sensing Data Fusion to Land Use Mapping and Monitoring. *Remote Sensing* **2016**, *8*, 70, doi:10.3390/rs8010070.
42. STEP *Sen2Cor*; 2022;
43. Huete, A.R. A Soil-Adjusted Vegetation Index (SAVI). *Remote Sensing of Environment* **1988**, *25*, 295–309, doi:10.1016/0034-4257(88)90106-X.
44. McFEETERS, S.K. The Use of the Normalized Difference Water Index (NDWI) in the Delineation of Open Water Features. *International Journal of Remote Sensing* **1996**, *17*, 1425–1432, doi:10.1080/01431169608948714.
45. Fisser, H. GitHub, Truck Detection Sentinel2 COVID19 Available online: https://github.com/hfisser/Truck_Detection_Sentinel2_COVID19 (accessed on 13 May 2022).
46. Zha, Y.; Gao, J.; Ni, S. Use of Normalized Difference Built-up Index in Automatically Mapping Urban Areas from TM Imagery. *International Journal of Remote Sensing* **2003**, *24*, 583–594, doi:10.1080/01431160304987.
47. Zhou, T.; Fu, H.; Sun, C.; Wang, S. Shadow Detection and Compensation from Remote Sensing Images under Complex Urban Conditions. *Remote Sensing* **2021**, *13*, 699, doi:10.3390/rs13040699.
48. Tsai, V.J.D. A Comparative Study on Shadow Compensation of Color Aerial Images in Invariant Color Models. *IEEE Trans. Geosci. Remote Sensing* **2006**, *44*, 1661–1671, doi:10.1109/TGRS.2006.869980.
49. CORINE Land Cover Available online: https://www.eea.europa.eu/publications/COR0-landcover (accessed on 19 September 2018).
50. O'Malley, T.; Bursztein, E.; Long, J.; Chollet, F.; Jin, H.; Invernizzi, L. KerasTuner Available online: https://github.com/keras-team/keras-tuner.
51. Sokolova, M.; Lapalme, G. A Systematic Analysis of Performance Measures for Classification Tasks. *Information Processing & Management* **2009**, *45*, 427–437, doi:10.1016/j.ipm.2009.03.002.
52. Tharwat, A. Classification Assessment Methods. *ACI* **2021**, *17*, 168–192, doi:10.1016/j.aci.2018.08.003.
53. Vieira, A.J.; Garrett, J.M. Understanding Interobserver Agreement: The Kappa Statistic. *Fam. Med.* **2005**, 360–363.
54. Landis, J.R.; Koch, G.G. The Measurement of Observer Agreement for Categorical Data. *Biometrics* **1977**, *33*, 159, doi:10.2307/2529310.